ACS APPLIED MATERIALS & INTERFACES

Research Article

www.acsami.org

Three-Dimensional Porous Supramolecular Architecture from Ultrathin g-C_3N_4 Nanosheets and Reduced Graphene Oxide: Solution Self-Assembly Construction and Application as a Highly Efficient Metal-Free Electrocatalyst for Oxygen Reduction Reaction

Jingqi Tian,[†,‡] Rui Ning,[†,‡] Qian Liu,[†] Abdullah M. Asiri,[§,∥] Abdulrahman O. Al-Youbi,[§,∥] and Xuping Sun*[,†,‡,§,∥]

[†]State Key Lab of Electroanalytical Chemistry, Changchun Institute of Applied Chemistry, Chinese Academy of Sciences, Changchun 130022, Jilin, China

[‡]Graduate School of the Chinese Academy of Sciences, Beijing 100039, China

[§]Department of Chemistry, Faculty of Science, King Abdulaziz University, Jeddah 21589, Saudi Arabia

[∥]Center of Excellence for Advanced Materials Research, King Abdulaziz University, Jeddah 21589, Saudi Arabia

Supporting Information

ABSTRACT: Direct mixing of aqueous dispersions of ultrathin g-C_3N_4 nanosheets and graphene oxide (GO) under ultrasonication leads to three-dimensional (3D) porous supramolecular architecture. Photoreduction of GO yields conductive porous g-C_3N_4/rGO hybrid. The resulting 3D architecture possesses high surface area, multilevel porous structure, good electrical conductivity, efficient electron transport network, and fast charge transfer kinetics at g-C_3N_4/rGO interfaces, which facilitate the diffusion of O_2, electrolyte, and electrons in the porous frameworks during oxygen reduction reaction (ORR). Ultrathin g-C_3N_4 nanosheet also causes effective electron tunneling through g-C_3N_4 barrier, leading to rich electrode−electrolyte−gas three-phase boundaries, and shortens the electron diffusion distance from rGO to O_2. As a novel ORR catalyst, such 3D hybrid exhibits remarkable catalytic performance, outperformed other g-C_3N_4/rGO composites, and exhibits excellent durability.

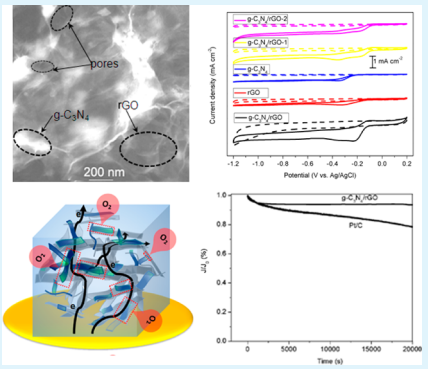

KEYWORDS: *ultrathin g-C_3N_4 nanosheets, graphene, photoreduction, 3D porous supramolecular architecture, oxygen reduction reaction, electrocatalyst*

INTRODUCTION

Fuel cells are an attractive clean energy technology with low or zero emissions from operation. However, the kinetic sluggishness of the oxygen reduction reaction (ORR) limits the performance of fuel cells. As such, the exploration of highly active catalysts for four-electron ($4e^-$) ORR is of prime importance to optimize the performance of the fuel cell.[1−4] Although Pt-based materials have been developed as catalyst for ORR since its first use in the 1960s,[5] high cost, resource scarcity, and poor methanol tolerance restricted their widespread commercialization of fuel cells. Thus, many approaches have been developed to reduce or replace Pt-based materials, such as using less active precious metals,[6] nonprecious catalysts,[7] or enzymatic catalysts,[8] etc.

Recently, nitrogen-containing carbon materials have been of particular interest as metal-free electrocatalysts for ORR;[1,9−11] however, they suffer from low and unstable catalytic activity due to the low level of nitrogen concentration.[12] Graphitic carbon nitride (g-C_3N_4) possesses high nitrogen content with excellent chemical and thermal stability.[13] In addition, g-C_3N_4 is environmentally friendly, is sustainable, and can be facilely synthesized in large scale with low cost. Early studies revealed that g-C_3N_4 suffers from extremely low electrical conductivity and has relatively low ORR catalytic activity.[14] Such issue can be solved by using conductive carbon including carbon black,[14,15] graphene,[16,17] and mesoporous[12] or macroporous carbon[18] as a support which favors the $4e^-$ ORR process and improves the performance of the catalyst. However, in situ immobilization technique used in previous studies gives no control over g-C_3N_4 thickness on one hand and also might lead to fully covered carbon blocking electron transport pathways between g-C_3N_4/C composite catalysts on the other hand.

An ideal g-C_3N_4/C composite ORR electrocatalyst should meet the following requirements: (1) carbon support should have high surface area and good electrical conductivity;[18] (2) g-C_3N_4 should be as thin as possible and easily accessed by electrolyte and O_2; (3) close electron coupling between g-C_3N_4 and carbon should be established; (4) there should be efficient

Received: October 15, 2013
Accepted: December 30, 2013
Published: December 30, 2013

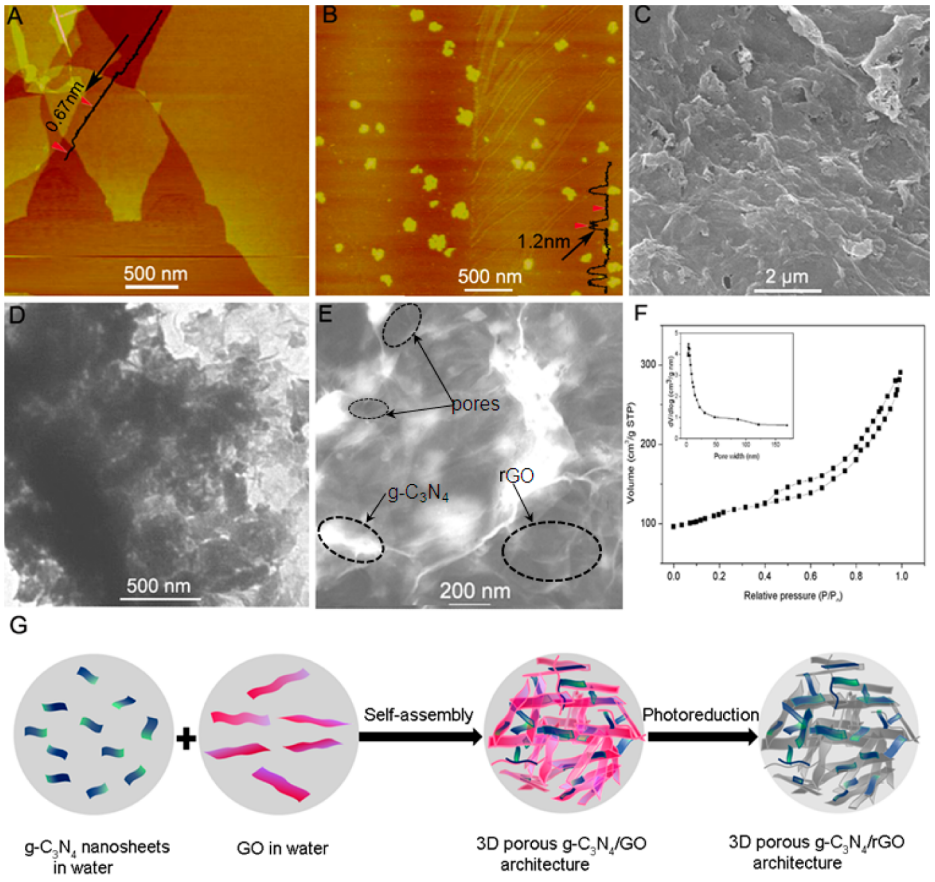

Figure 1. AFM images of (A) GO and (B) g-C_3N_4 nanosheets used for self-assembly (inset, the corresponding section analysis). (C) SEM and (D) TEM images of the assemblies of g-C_3N_4 and GO nanosheets. (E) STEM image of g-C_3N_4/rGO hybrid. (F) Nitrogen adsorption/desorption isotherm and the BJH pore-size distribution curve (inset) of g-C_3N_4/rGO hybrid. (G) Schematic diagram to illustrate the fabrication process of 3D porous supramolecualr architecture of g-C_3N_4 nanosheets and rGO.

electron transport network among composite catalysts. Particularly, the porosity of catalyst plays an important role in fuel cell, it is also of critical importance to develop porous catalyst.[12,19,20] Solution self-assembly provides a powerful and universal strategy for bottom-up construction of three-dimensional (3D) porous functional architectures;[21,22] however, its application for designing C-integrated g-C_3N_4 composite ORR catalyst has been never addressed before.

In this paper, we constructed a 3D porous supramolecular architecture from ultrathin g-C_3N_4 nanosheets and graphene oxide (GO) via solution self-assembly route. Subsequent photoreduction of GO using g-C_3N_4 as a photocatalyst leads to porous g-C_3N_4/reduced GO (g-C_3N_4/rGO) hybrid with good electrical conductivity. As a novel ORR catalyst, the 3D hybrid shows that remarkable catalytic performance outperformed single component, physical mixed, or in situ immobilized composite or previously reported g-C_3N_4/C composites, with excellent durability, and the possible mechanism involved is also discussed. Using Co-doped g-C_3N_4 nanosheets gives a 3D composite catalyst with greatly improved ORR activity comparable to current nitrogen-doped carbon catalysts.

EXPERIMENTAL SECTION

Materials. KOH (Beijing Chemical Corp), HCl (36 wt %, Beijing Chemical Corp), methanol (Beijing Chemical Corp), $Co(OAc)_2 \cdot 4H_2O$ (Beijing Chemical Corp), $KMnO_4$ (Beijing Chemical Corp), melamine (Aladdin Ltd. (Shanghai, China)), H_2O_2 (30 wt %, Aladdin Ltd. (Shanghai, China), graphite powder (Aladdin Ltd. (Shanghai, China)), H_2SO_4 (Aladdin Ltd. (Shanghai, China)), $NaNO_3$ (Aladdin Ltd. (Shanghai, China)), Pt/C (20 wt % Pt on Vulcan XC-72R, Sigma-Aldrich), and Nafion (5 wt %, Sigma-Aldrich) were used as received.

Preparation of Ultrathin g-C_3N_4 Nanosheets. Bulk g-C_3N_4 was first synthesized by pyrolyzation of melamine. Briefly, 10 g of melamine was heated to 600 °C in 190 min and maintained at this temperature for 2 h. Bulk Co-g-C_3N_4 was made through the same procedure with heating of the mixture of $Co(OAc)_2 \cdot 4H_2O$ (15 mg) and melamine (100 mg) to 600 °C and maintenance at this temperature for 2 h. Ultrathin g-C_3N_4 nanosheets were prepared via ultrasonication-assisted liquid exfoliating of as-prepared bulk g-C_3N_4.[23−26] Typically, bulk g-C_3N_4 powder (10 mg) was dispersed in water (10 mL) followed by consecutive sonication for 10 h. The unexfoliated g-C_3N_4 was removed by centrifugation.

Preparation of GO and rGO. GO was synthesized according to a modified Hummer's method.[27] rGO was prepared according to our previous work.[28]

Synthesis of 3D Porous g-C_3N_4/rGO, g-C_3N_4/rGO-1, g-C_3N_4/rGO-2, and Co-g-C_3N_4/rGO. An amount of 10 mL of g-C_3N_4 nanosheets suspension was mixed with 0.325 mL of GO (0.5 mg mL^{-1}) aqueous solution with weight ratio of 8:1 of g-C_3N_4 to GO under ultrasonication for 30 min. After that, the mixture was under illumination after the addition of methanol with a xenon lamp (CHFXQ500W, Beijing, China) after degassing of oxygen. The product was washed with water by centrifugation several times. The precipitate was redispersed in H_2O (4 mg mL^{-1}) for further use. Co-g-C_3N_4/rGO was synthesized according the same procedure except Co-g-C_3N_4 was used instead of g-C_3N_4. g-C_3N_4/rGO-1 was prepared by physical mixture of rGO and bulk g-C_3N_4. g-C_3N_4/rGO-2 was prepared by in situ immobilization technique. Typically, 4.2 mg of

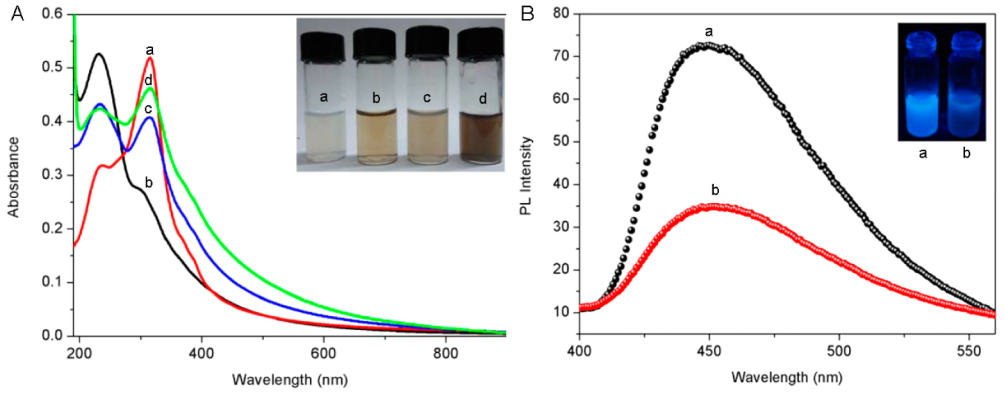

Figure 2. (A) UV−vis absorption spectra and corresponding photographs (inset) of aqueous dispersions of g-C_3N_4 nanosheets (a), GO (b), g-C_3N_4/GO (c), and g-C_3N_4/rGO (d). (B) PL spectra and photographs of aqueous dispersion of g-C_3N_4 nanosheets in the absence (a) and presence (b) of GO under illumination (excitation, 365 nm).

dicyandiamide was dissolved in 0.325 mL of GO (0.5 mg mL^{-1}) aqueous solution and the mixture was dried at 80 °C for 12 h. The resulting powder was then heated to 600 °C in 190 min and maintained at 600 °C for 4 h.

Characterizations. MultiMode-V (Veeco Metrology, Inc.) was used for atomic force microscopy (AFM) characterizations. The structures of the samples were determined by scanning electron microscopy (SEM) performed on a (Philips XL30 ESEM FEG) scanning electron microscope. The optical absorption spectra of the samples were recorded in a UV−visible spectrophotometer (Shimadzu, Japan). A RF-5301PC spectrofluorometer (Shimadzu, Japan) was applied to collect fluorescent emission spectra. Transmission electron microscopy (TEM) images were taken on a HITACHI H-8100 electron microscopy (Hitachi, Tokyo, Japan) operated at 200 kV. N_2 adsorption and desorption isotherms were obtained on a Quantachrome NOVA 1000 system at liquid N_2 temperature. The X-ray photoelectron spectroscopy (XPS) measurements were performed using an ESCALABMK II X-ray photoelectron spectrometer with the exciting source of Mg. Powder X-ray diffraction (XRD) patterns were collected using a RigakuD/MAX 2550 diffractmeter with Cu Kα radiation (λ = 1.5418 Å). Electrochemical measurements are performed under identical conditions. The data were collected using a CHI 660D electrochemical analyzer (CH Instruments, Inc., Shanghai, China). The electrode kinetics measurements were carried out using a glassy carbon electrode (GCE, geometric area of 0.196 cm^2). The reference electrode was an Ag/AgCl electrode and a platinum wire as the counter electrode. To prepare the working electrode, the catalyst (4 mg) and Nafion solution (5 wt %, 10 μL) were mixed in water (1 mL). For Pt/C ink preparation, Pt/C (2 mg), EtOH (500 μL), and Nafion solution (5 wt %, 17.5 μL) were mixed together. Then 15 μL of the catalyst ink was dipped onto a glassy carbon electrode (diameter: 5 mm) with loading amount of 0.3 mg/cm^2.

Calculation of Electrochemical Active Surface Area (EASA). The EASA of bare GCE was calculated according to the literature, and the value is 0.2 cm^2, which is well consistent with value provided by the company (0.196 cm^2). The EASA of the g-C_3N_4/rGO hybrid modified electrodes were calculated based on the double-layer capacitor according to the literature. The cyclic voltammograms (CVs) with different amounts of g-C_3N_4/rGO hybrids on GCE and the relationship between the capacitor and the loaded catalyst amounts are shown in Figure S1 of Supporting Information. It can be confirmed that the capacitors of g-C_3N_4/rGO hybrid modified electrodes show a linear relationship with their EASA. The EASA of the g-C_3N_4/rGO modified electrode (0.3 mg cm^{-2}) was calculated to be 9.02 cm^2. Similar calculations are applied for g-C_3N_4. The EASA of g-C_3N_4 modifed electrode (0.3 mg cm^{-2}) is 2.36 cm^2.

RESULTS AND DISCUSSION

Figure 1A and Figure 1B show the AFM images of the GO and g-C_3N_4 used for assembly, respectively, indicating their 2D nature. The GO was about 0.67 nm in thickness. The thickness of the g-C_3N_4 was about 1.2 nm, indicating formation of ultrathin g-C_3N_4 nanosheets after ultrasonication treatment of bulk g-C_3N_4.[21−24] In order to verify the formation of the g-C_3N_4, the as-prepared sample was characterized by XRD. In Figure S2A, the XRD pattern of g-C_3N_4 confirms a graphitic-like layer structure. A strong diffraction peak at 27.35°, typically corresponding to the (002) interplanar distance of 0.326 nm, is well-known for the melon neworks.[29] XPS analysis was also carried out. The high-resolution N 1s spectrum of g-C_3N_4 displays typical heptazine repeating units with several N species, including pyridinic N (N_{2C}, 398.3 eV), tertiary N (N_{3C}, 399.5 eV), amino functions (−NH_2, 401.4 eV), and *N*-oxide (403.8 eV),[30] as shown in Figure S2B. The lateral sizes of GO and g-C_3N_4 were typically in the range from 0.5 to several μm and from 100 to 250 nm, respectively. The mixing of aqueous dispersions of g-C_3N_4 and GO under ultrasonication leads to many precipitates. The SEM image of the precipitates suggests they are porous microstructures (Figure 1C). Energy-dispersive spectrometry (EDS) was used to analyze the composition of the composites (Figure S3). The observation of peaks corresponding to C, O, N (other peaks are assigned to the substrate and sputtered Au) indicates that the microstructure is assembled from GO and g-C_3N_4. The TEM image reveals that the microstructure consists of many GO and g-C_3N_4 nanosheets, as shown in Figure 1D. The scanning TEM (STEM) image (Figure S4) not only provides clear distinction between g-C_3N_4 and GO nanosheets but also indicates the partial coverage of GO by g-C_3N_4 and the presence of macropores in the frameworks. A green photoreduction strategy was further utilized to reduce GO to form g-C_3N_4/rGO hybrid using g-C_3N_4 as a photocatalyst. Figure 1E shows the STEM image of the g-C_3N_4/rGO hybrid, suggesting the preservation of the macroporous nature after photoreduction. Figure 1F shows the nitrogen adsorption−desorption isotherm for the hybrids. The inset was the Barrett−Joyner−Halenda (BJH) pore-size distribution curve of the hybrid. The measured Brunauer−Emmett−Teller (BET) area is 310 m^2 g^{-1}, which is much higher than that of g-C_3N_4 nanosheets (16.2 m^2 g^{-1}) and bulk g-C_3N_4 (7.94 m^2 g^{-1}).[25] Moreover, besides a broad peak ranging from 50 to 100 nm due to macropores, a sharp one at 5 nm is also observed in the BJH pore-size distribution curve. All

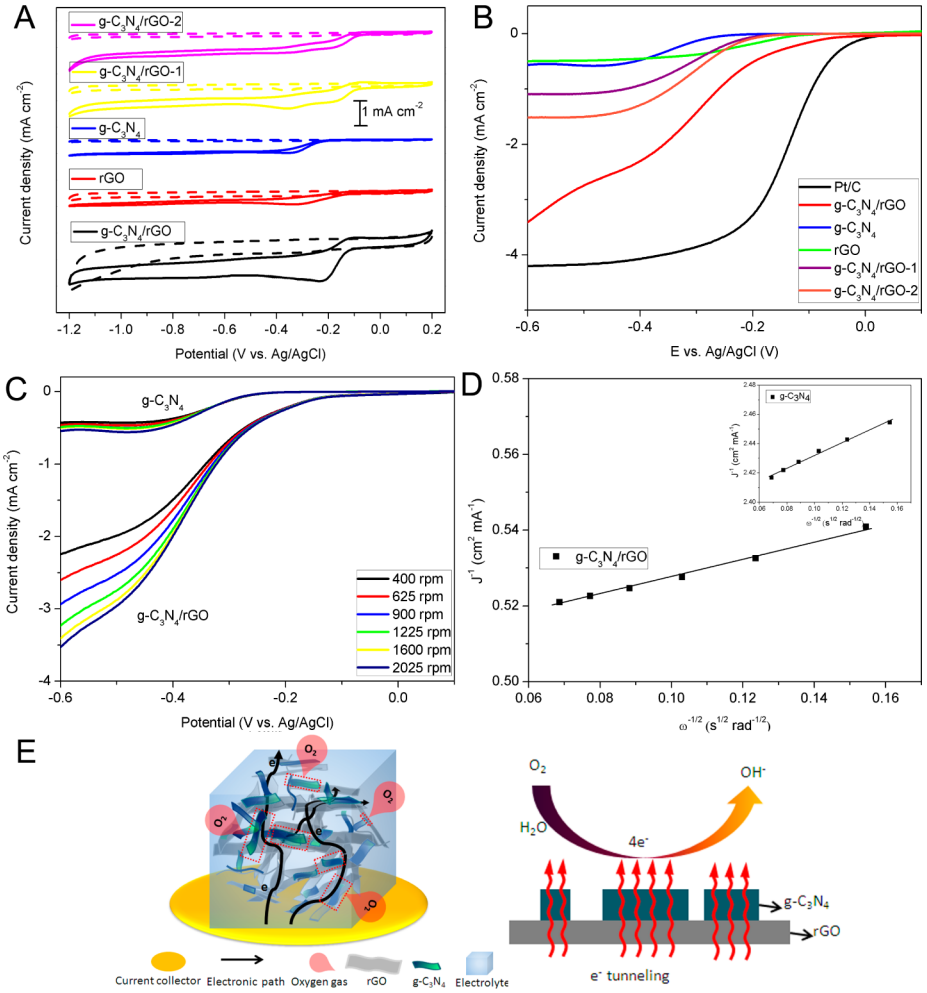

Figure 3. (A) CVs of g-C_3N_4, rGO, g-C_3N_4/rGO, g-C_3N_4/rGO-1, and g-C_3N_4/rGO-2 on GCEs in O_2-saturated (solid line) or N_2-saturated (dashed line) 0.1 M KOH. (B) LSVs of g-C_3N_4, rGO, g-C_3N_4/rGO, g-C_3N_4/rGO-1, g-C_3N_4/rGO-2, and Pt/C catalysts on RDEs at 1600 rpm in KOH (0.1 M, O_2-saturated) at a sweep rate of 5 mV/s after the correction of capacitive current. (C) LSVs of g-C_3N_4 and g-C_3N_4/rGO on RDEs in KOH (O_2-saturated 0.1 M) with various rotation rates at a scan rate of 5 mV/s. (D) Koutecky–Levich plots of g-C_3N_4/rGO and g-C_3N_4 (inset) at −0.4 V. (E) Schematic diagram illustrating (left) the diffusion pathways of O_2, electrolyte, and electrons within 3D porous g-C_3N_4/rGO architecture during ORR with marked rectangular regions representing TPBs and (right) the effective electron diffusion from rGO to O_2 through g-C_3N_4 barrier via electron tunneling mechanism.

these results confirm the formation of 3D porous g-C_3N_4/rGO architecture. Figure 1G is a schematic diagram illustrating the whole fabrication process. It is believed that the π-stacking interactions between the sp^2 lattice of g-C_3N_4 and the sp^2 graphene lattice as well as the hydrogen-bonding interactions between the nitrogen-containing groups in g-C_3N_4 and oxygen functional group of GO are responsible for the self-assembly formation of the 3D porous frameworks in solution. It was found that the 3D hybrid was always obtained from g-C_3N_4 and GO, even when different weight ratios were used for the assembly. However, the use of rGO or graphene sheet without oxygen functional groups on its basal plane only leads to 2D hybrid.[27]

Figure 2A exhibits the UV–vis absorption spectra of g-C_3N_4 nanosheets, GO, g-C_3N_4/GO, and g-C_3N_4/rGO aqueous solutions (inset, correspinding photographs). g-C_3N_4 shows a shoulder peak at ∼230 nm and a sharp peak at ∼306 nm (curve a). GO exhibits a shoulder peak at ∼300 nm and a sharp peak at ∼230 nm.[31] In the presence of GO, the absorption band of g-C_3N_4 moved to 310 nm, attributed to the assembly of g-C_3N_4 and GO due to π–π stacking[32] and hydrogen-bonding interactions between them. It was reported that GO is a very efficient quencher of fluorescence if they are close enough.[33] Indeed, the presence of GO also leads to strong fluorescence quenching of g-C_3N_4 (Figure 2B). After irradiation, the peak at 230 nm broadens and decreases in intensity with the increase of overall light region absorption. All these observations indicate the regaining of the π-conjugation network in GO.[32] Note that because of the heavy overlap of the absorption peaks of g-C_3N_4 and GO, it is very difficult for us to identify photoreduction-induced red shift and disappearance of the peak at 230 and 300 nm of GO, respectively.[31] Note that a 10 min irradiation leads to a change of solution color from yellow to black (inset) but almost no color change occurs for the control sample without the presence of g-C_3N_4, further confirming that GO has been reduced and indicating that g-C_3N_4 serves as a powerful reductant in GO photoreduction. Four-probe measurement shows that the g-C_3N_4/rGO hybrid has a dc conductivity of approximately 10.5 S cm^{-1}.

Figure 3A shows the CVs of g-C_3N_4 nanosheet, rGO, g-C_3N_4/rGO on GCEs in O_2-saturated (solid line) or N_2-saturated (dashed line) 0.1 M KOH. No characteristic peak in

dx.doi.org/10.1021/am404536w | ACS Appl. Mater. Interfaces 2014, 6, 1011–1017

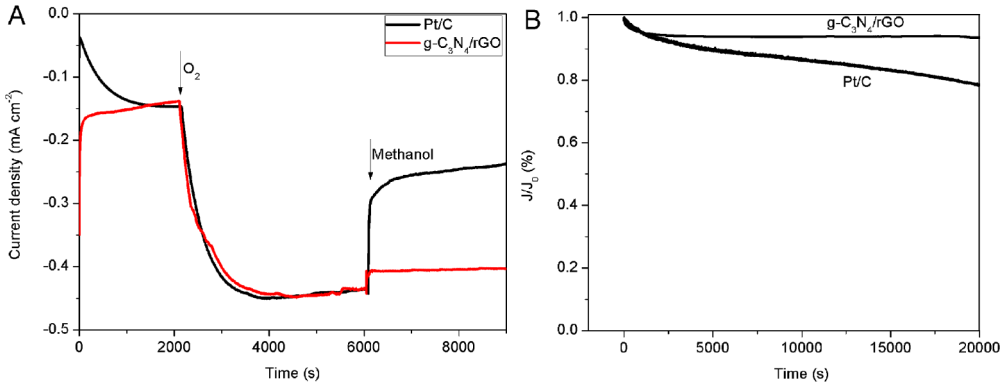

Figure 4. (A) Chronoamperometric responses of g-C_3N_4/rGO and 20% Pt/C at −0.30 V vs Ag/AgCl in KOH (0.1 M, O_2-saturated). The arrows represent the addition of O_2 and methanol. (B) Chronoamperometric responses for ORR on g-C_3N_4/rGO and Pt/C catalysts at −0.3 V and 1600 rpm in KOH (0.1 M, O_2-saturated) solution.

this potential window is observed for g-C_3N_4/rGO in N_2-saturated solution. Thus, the reduction peak observed in O_2-saturated solution for g-C_3N_4/rGO can be attributed to the ORR process. g-C_3N_4 shows two obvious ORR peaks at −0.32 and −0.78 V, corresponding to two separate reduction processes.[7] rGO also shows certain ORR catalytic activity with onset and peak potentials of −0.12 and −0.30 V, respectively. In contrast, g-C_3N_4/rGO shows a single ORR peak at −0.21 V, which is ∼90 mV more positive than that of rGO. Moreover, the wave current of g-C_3N_4/rGO is also enhanced by 1.6 and 2.3 times compared with g-C_3N_4 and rGO, respectively. For comparison study, another two control samples were prepared by physical mixing of bulk g-C_3N_4 and rGO (g-C_3N_4/rGO-1) and in situ immobilization of g-C_3N_4 on rGO (g-C_3N_4/rGO-2). During the preparation of g-C_3N_4/rGO and the control samples of g-C_3N_4/rGO-1 and g-C_3N_4/rGO-2, there are many different factors including the type of precursor and reduction method that can affect the formation of the samples. These factors could lead to the possible difference in the graphitic character, C/N ratio, and C−N coordination environment which consequently affect the ORR activity. Thus, the samples were synthesized via optimizations to minimize the difference, and the ORR activities between them can be compared. The XRD patterns show a broad diffraction peak at 26.9° for g-C_3N_4/rGO-1 and g-C_3N_4/rGO-2 (Figure S5A), indicating that both control samples have a layer-to layer distance (0.334 nm) between that of rGO (0.340 nm) and g-C_3N_4 (0.323 nm). The XPS survey spectra of both samples (Figure S5B) show the existence of C and N in the samples with similar C/N ratio. The high-resolution N 1s spectra of both samples (Figure S5C and S5D) display typical heptazine repeating units with several N species, including pyridinic N (N_{2C}, 398.3 eV), tertiary N (N_{3C}, 399.5 eV), amino functions (−NH_2, 401.4 eV), and *N*-oxide (403.8 eV),[30] indicating that the C−N coordination environment in both samples is the same as that in g-C_3N_4/rGO. Both samples show two ORR peaks at relatively lower peak potentials than g-C_3N_4/rGO. Figure 3B shows the linear sweep voltammograms (LSVs) of g-C_3N_4, rGO, g-C_3N_4/rGO, g-C_3N_4/rGO-1, g-C_3N_4/rGO-2, and commercial Pt/C catalysts measured on rotating disk electrodes (RDEs). From the LSV obtained on g-C_3N_4, the current plateau has not been found and only a reduction peak at −0.49 V is observed, demonstrating a $2e^-$ reduction process. In contrast, g-C_3N_4/rGO shows a broad current plateau, attributed to the $4e^-$ dominated process.[12] Compared with other catalysts except Pt/C, g-C_3N_4/rGO shows lower onset potential and higher current density. These results suggest that g-C_3N_4/rGO exhibits superior ORR catalytic activity over single component, physical mixed, or in situ immobilized composite. Table S1 shows a comparison of the ORR peak and onset potentials of g-C_3N_4/rGO and previously reported g-C_3N_4/C composites, revealing that g-C_3N_4/rGO possesses higher ORR performance. Note that although the onset potential of g-C_3N_4/rGO is −0.12 V more negative than that of Pt/C catalyst, the ORR current density at −0.6 V of g-C_3N_4/rGO is comparable with that of Pt/C. The CVs of different catalysts were also normalized by the loading weight (Figure S8). It is important to state that assembly of Co-doped g-C_3N_4 (Co-g-C_3N_4) nanosheet, obtained similarly by exfoliation of bulk Co-g-C_3N_4, and GO gives a 3D composite catalyst with greatly improved ORR activity (Figure S6) comparable to current nitrogen-doped carbon catalysts,[11,34−38] which can be attributed to the available Co−N_x active sites[17] and the intrinsic ORR activity of Co^{2+} species contained therein.[39] In order to verify the formation of Co-g-C_3N_4, the as-prepared sample was characterized by XRD. In Figure S7A, the XRD pattern shows a significant decrease in intensity and broading of the (002) peak compared with that of g-C_3N_4. The XPS survey spectrum of Co-g-C_3N_4 (Figure S7B) shows the existence of C, N, Co in the sample, indicating the formation of Co-g-C_3N_4. The high-resolution N 1s spectrum of Co-g-C_3N_4 displays typical heptazine repeating units with several N species, including pyridinic N (N_{2C}, 398.3 eV), tertiary N (N_{3C}, 399.5 eV), amino functions (−NH_2, 401.4 eV), and *N*-oxide (403.8 eV),[30] as shown in Figure S7C, indicating that the framework of g-C_3N_4 is not changed with the inclusion of Co species. The N 1s BE value of the reported Co−N_x material lies at ∼399 eV.[40] The Co 2p spectra is presented in Figure S7D. The peaks at 781.2 and 783.4 eV can be ascribed to the Co(II) state in the form of Co−N_x[17] and the excessive Co ions.[40]

Figure 3C presents the LSVs obtained at different rotating speeds for g-C_3N_4 and g-C_3N_4/rGO to reveal the ORR kinetics. The electron transfer numbers (n) of g-C_3N_4 and g-C_3N_4/rGO calculated from the Koutechy−Levich plots is 2.4 and 3.8, respectively (Figure 3D), demonstrating a combined pathway of $2e^-$ and $4e^-$ processes on g-C_3N_4 and $4e^-$ dominated ORR process on g-C_3N_4/rGO.

The high ORR catalytic performance of the 3D porous g-C_3N_4/rGO hybrid can be rationally explained as follows. It was reported that g-C_3N_4 only has limited electron transport ability,

dx.doi.org/10.1021/am404536w | ACS Appl. Mater. Interfaces 2014, 6, 1011−1017

resulting in an inefficient $2e^-$ ORR pathway and hence relatively low ORR catalytic activity.[12] Although GO used for assembly is insulating, the photoreducion process leads to conductive 3D architectures. The integrated g-C_3N_4 nanosheets as ORR active centers open up the interlayer space of densely stacked rGO, giving porous architecture. The rGO sheets serve as "highways" for electron transport, and the partial coverage of rGO surface by g-C_3N_4 facilitates direct electrical contacts between neighboring rGO sheets in the composite, providing an efficient 3D electron transport network and thus promoting electron transport in the composite catalyst. The close electron coupling between g-C_3N_4 and rGO also leads to fast charge transfer at the interfaces of g-C_3N_4/rGO. All these facilitate the diffusion of O_2, electrolyte, and electrons in the porous frameworks during ORR. Although g-C_3N_4 has low electrical conductivity, given that electrons can tunnel over relatively large distance of 3 nm [41] and the g-C_3N_4 nanosheet used is only about 1.2 nm in thickness, electrons can effectively tunnel through the g-C_3N_4 barrier,[42] leading to rich electrode−electrolyte−gas three-phase boundaries (TPBs). The ultrathin thickness of g-C_3N_4 nanosheet also shortens the electron diffusion distance from rGO to O_2. As a result, a high ORR catalytic activity is achieved on the 3D porous supramolecular g-C_3N_4/rGO hybrid. Figure 3E shows a schematic diagram to illustrate the diffusion pathways of O_2, electrolyte, and electrons within 3D porous g-C_3N_4/rGO architecture during ORR and the effective electron diffusion from rGO to O_2 through g-C_3N_4 barrier via electron tunneling mechanism.

In fuel cells, the catalytic selectivity against the oxidation is critical for cathode materials, which has been a big problem for Pt-based catalysts, and the electrocatalytic sensitivity of g-C_3N_4/rGO against the electrooxidation of methanol in ORR was also tested and compared with commercial Pt/C catalyst. Upon the addition of methanol, g-C_3N_4/rGO retains a stable response of its initial ORR current under −0.3 V (Figure 4A), suggesting its good tolerance of methanol. In contrast, the current is sharply decreased for the Pt/C catalyst, indicating the oxidation of methanol and poisoning of the catalyst. Such observations show that g-C_3N_4/rGO possesses a better tolerance toward methanol poisoning. The durability of the catalyst was also measured. The g-C_3N_4/rGO shows a decrease of 7% in current density over 20 000 s of continuous operation, while a decrease of 35% in current density for Pt/C catalyst is observed (Figure 4B). This result indicates that g-C_3N_4/rGO has superior durability over Pt/C catalyst, owing to the excellent stability of g-C_3N_4 as well as the strong interactions and good electrical contact between g-C_3N_4 and rGO in the frameworks.

CONCLUSION

In summary, a novel 3D porous supramolecular architecture of ultrathin g-C_3N_4 nanosheets and rGO has been successfully constructed by solution self-assembly of g-C_3N_4 and GO followed by photoreduction catalyzed by g-C_3N_4. The resulting 3D hybrid possesses high surface area, multilevel porous structure, good electrical conductivity, efficient electron transport network, and fast charge transfer kinetics at g-C_3N_4/rGO interfaces. Ultrathin g-C_3N_4 nanosheet also allows effective electron tunneling through g-C_3N_4 barrier leading to rich TPBs and shortens electron diffusion distance from rGO to O_2. The 3D porous hybrid as a metal-free ORR electrocatalyst thus exhibits superior catalytic performance over other g-C_3N_4/C composites with excellent durability. Furthermore, the use of Co-g-C_3N_4 alternative gives a 3D composite catalyst with catalytic activity comparable to that of current nitrogen-doped carbon catalysts. The present work is significant because it is the first demonstration of using self-assembly and photoreduction for the simple and low-cost construction of 3D porous g-C_3N_4/C composite ORR catalysts with high efficiency. Moreover, this hybrid may hold great promise as a highly efficient catalyst in alkaline fuel cells and metal−air batteries.[43]

ASSOCIATED CONTENT

Supporting Information

EDS spectra of the g-C_3N_4/rGO hybrid; STEM image of g-C_3N_4/GO hybrid; Table S1; XRD pattern, XPS spectra, CV, and LSV of Co-g-C_3N_4/rGO; XRD pattern and XPS spectra of g-C_3N_4/rGO-1 and g-C_3N_4/rGO-2; CVs of g-C_3N_4/rGO hybrids; CVs of different catalysts normalized by loading weight. This material is available free of charge via the Internet at http://pubs.acs.org.

AUTHOR INFORMATION

Corresponding Author

*Phone/fax: 0086-431-85262065. E-mail: sunxp@ciac.jl.cn.

Notes

The authors declare no competing financial interest.

ACKNOWLEDGMENTS

This work was supported by the National Natural Science Foundation of China (Grant 21175129), the National Basic Research Program of China (Grant 2011CB935800), and the Scientific and Technological Development Plan Project of Jilin Province (Grants 20100534 and 20110448).

REFERENCES

(1) Gong, K.; Du, F.; Xia, Z.; Durstock, M.; Dai, L. *Science* **2009**, *323*, 760−764.
(2) Snyder, J.; Fujita, T.; Chen, M.; Erlebacher, J. *Nat. Mater.* **2010**, *9*, 904−907.
(3) Lefevre, M.; Proietti, E.; Jaouen, F.; Dodelet, J. P. *Science* **2009**, *324*, 71−74.
(4) Tang, H.; Yin, H.; Wang, J.; Yang, N.; Wang, D.; Tang, Z. *Angew. Chem., Int. Ed.* **2013**, *52*, 5585−5589.
(5) Alkali Fuel Cell History. http://americanhistory.si.edu/fuelcells/alk/alk3.htm (Copyright 2001, Smithsonian Institution).
(6) Zhang, J.; Sasaki, K.; Sutter, E.; Adzic, R. R. *Science* **2007**, *315*, 220−222.
(7) Bashyam, R.; Zelenay, P. *Nature* **2006**, *443*, 63−66.
(8) Collman, J. P.; Devaraj, N. K.; Decreau, R. A.; Yang, Y.; Yan, Y.; Ebina, W.; Eberspacher, T. A.; Chidsey, C. E. D. *Science* **2007**, *315*, 1565−1568.
(9) Tang, Y.; Allen, B. L.; Kauffman, D. R.; Star, A. *J. Am. Chem. Soc.* **2009**, *131*, 13200−13201.
(10) Qu, L.; Liu, Y.; Baek, J. B.; Dai, L. *ACS Nano* **2010**, *4*, 1321−1326.
(11) Liu, R.; Wu, D.; Feng, X.; Müllen, K. *Angew. Chem., Int. Ed.* **2010**, *49*, 2565−2569.
(12) Zheng, Y.; Jiao, Y.; Chen, J.; Liu, J.; Liang, J.; Du, A.; Zhang, W.; Zhu, Z.; Smith, S. C.; Jaroniec, M.; Lu, G.; Qiao, S. *J. Am. Chem. Soc.* **2011**, *133*, 20116−20119.
(13) Groenewolt, M.; Antonietti, M. *Adv. Mater.* **2005**, *17*, 1789−1792.
(14) Lyth, S. M.; Nabae, Y.; Moriya, S.; Kuroki, S.; Kakimoto, M.; Ozaki, J.; Miyata, S. *J. Phys. Chem. C* **2009**, *113*, 20148−20151.
(15) Lyth, S. M.; Nabae, Y.; Islam, N. M.; Kuroki, S.; Kakimoto, M.; Miyata, S. *J. Electrochem. Soc.* **2011**, *158*, B194−B201.

(16) Sun, Y.; Li, C.; Xu, Y.; Bai, H.; Yao, Z.; Shi, G. *Chem. Commun.* **2010**, *46*, 4740−4742.
(17) Liu, Q.; Zhang, J. *Langmuir* **2013**, *29*, 3821−3828.
(18) Yang, S.; Feng, X.; Wang, X.; Müllen, K. *Angew. Chem., Int. Ed.* **2011**, *50*, 5339−5343.
(19) Liang, J.; Zheng, Y.; Chen, J.; Liu, J.; Hulicova-Jurcakova, D.; Jaroniec, M.; Qiao, S. *Angew. Chem., Int. Ed.* **2012**, *51*, 3892−3896.
(20) Kwon, K.; Sa, Y. J.; Cheon, J. Y.; Joo, S. H. *Langmuir* **2012**, *28*, 991−996.
(21) Innocenzi, P.; Malfatti, L.; Soler-Illia, G. J. A. A. *Chem. Mater.* **2011**, *23*, 2501−2509.
(22) Lee, Y. S., Ed. *Self-Assembly and Nanotechnology: A Force Balance Approach*; John Wiley & Sons: Hoboken, NJ, 2008.
(23) Zhang, X.; Xie, X.; Wang, H.; Zhang, J.; Pan, B.; Xie, Y. *J. Am. Chem. Soc.* **2013**, *135*, 18−21.
(24) Tian, J.; Liu, Q.; Asiri, A. M.; Al-Youbi, A. O.; Sun, X. *Anal. Chem.* **2013**, *85*, 5595−5599.
(25) Cheng, N.; Tian, J.; Liu, Q.; Ge, C.; Asiri, A. M.; Al-Youbi, A. O.; Sun, X. *ACS Appl. Mater. Interfaces* **2013**, *5*, 6815−6819.
(26) Tian, J.; Liu, Q.; Ge, C.; Xing, Z.; Asiri, A. M.; Al-Youbi, A. O.; Sun, X. *Nanoscale* **2013**, *5*, 8921−8924.
(27) Hummers, W. S., Jr.; Offeman, R. *J. Am. Chem. Soc.* **1958**, *80*, 1339.
(28) Tian, J.; Liu, S.; Zhang, Y.; Li, H.; Wang, L.; Luo, Y.; Asiri, A. M.; Al-Youbi, A. O.; Sun, X. *Inorg. Chem.* **2012**, *51*, 4742−4746.
(29) Yan, S.; Lv, S.; Li, Z.; Zou, Z. *Dalton Trans.* **2010**, *39*, 1488−1491.
(30) Zhao, Y.; Watanabe, K.; Hashimoto, K. *J. Am. Chem. Soc.* **2012**, *134*, 19528−19531.
(31) Liu, S.; Tian, J.; Wang, L.; Li, H.; Zhang, Y.; Sun, X. *Macromolecules* **2010**, *43*, 10078−10083.
(32) Li, H.; Liu, S.; Tian, J.; Wang, L.; Lu, W.; Luo, Y.; Asiri, A. M.; Al-Youbi, A. O.; Sun, X. *ChemCatChem* **2012**, *4*, 1079−1083.
(33) Lu, C.; Yang, H.; Zhu, C.; Chen, X.; Chen, G. *Angew. Chem., Int. Ed.* **2009**, *48*, 4785−4787.
(34) Yang, W.; Fellinger, T.-P.; Antonietti, M. *J. Am. Chem. Soc.* **2011**, *133*, 206−209.
(35) Chen, S.; Bi, J.; Zhao, Y.; Yang, L.; Zhang, C.; Ma, Y.; Wu, Q.; Wang, X.; Hu, Z. *Adv. Mater.* **2012**, *24*, 5593−5597.
(36) Dai, L.; Chang, D. W.; Baek, J.-B.; Lu, W. *Small* **2012**, *8*, 1130−1166.
(37) Li, H.; Kang, W.; Wang, L.; Yue, Q.; Xu, S.; Wang, H.; Liu, J. *Carbon* **2013**, *54*, 249−257.
(38) Ai, K.; Liu, Y.; Ruan, C.; Lu, L.; Lu, G. *Adv. Mater.* **2013**, *25*, 998−1002.
(39) Kent, C. A.; Concepcion, J. J.; Dares, C. J.; Torelli, D. A.; Rieth, A. J.; Miller, A. S.; Hoertz, P. G.; Meyer, T. J. *J. Am. Chem. Soc.* **2013**, *135*, 8432−8435.
(40) Morozan, A.; Jegou, P.; Jousselme, B.; Palacin, S. *Phys. Chem. Chem. Phys.* **2011**, *13*, 21600−21607.
(41) Duke, C.B., Ed. *Tunneling Phenomena in Solids*; Plenum Press: New York, 1969.
(42) Britnell, L.; Gorbachev, R. V.; Jalil, R.; Belle, B. D.; Schedin, F.; Katsnelson, M. I.; Eaves, L.; Morozov, S. V.; Mayorov, A. S.; Peres, N. M. R.; Castro Neto, A. H.; Leist, J.; Geim, A. K.; Ponomarenko, L. A.; Novoselov, K. S. *Nano Lett.* **2012**, *12*, 1707−1710.
(43) Armand, M.; Tarascon, J. M. *Nature* **2008**, *451*, 652−657.